International Journal of Heat and Mass Transfer 90 (2015) 323–338

Contents lists available at ScienceDirect

International Journal of Heat and Mass Transfer

journal homepage: www.elsevier.com/locate/ijhmt

Flow boiling and critical heat flux in horizontal channel with one-sided and double-sided heating

Chirag R. Kharangate [a], Lucas E. O'Neill [a], Issam Mudawar [a,*], Mohammad M. Hasan [b], Henry K. Nahra [b], Ramaswamy Balasubramaniam [b], Nancy R. Hall [b], Ashley M. Macner [b], Jeffrey R. Mackey [c]

[a] Boiling and Two-Phase Flow Laboratory (BTPFL), School of Mechanical Engineering, Purdue University, 585 Purdue Mall, West Lafayette, IN 47907, USA
[b] NASA Glenn Research Center, 21000 Brookpark Road, Cleveland, OH 44135, USA
[c] Vantage Partners, 3000 Aerospace Parkway, Brook Park, OH 44142, USA

ARTICLE INFO

Article history:
Received 14 February 2015
Received in revised form 22 June 2015
Accepted 23 June 2015
Available online 9 July 2015

Keywords:
Flow boiling
Critical heat flux
Gravity effects

ABSTRACT

This study explores flow boiling of FC-72 along a 5-mm high by 2.5-mm wide rectangular channel that is fitted with top and bottom heating walls. By activating one wall at a time, the opposing influences of gravity are examined for inlet velocities from 0.11 to 2.02 m/s. Results for top wall and bottom wall heating are then compared to those for double-sided heating. For top wall heating, high speed video imaging proves gravity effects are dominant at low velocities, accumulating vapor along the heated wall and resulting in low critical heat flux (CHF) values. For bottom wall heating, buoyancy aids in vapor removal and liquid replenishment of the heated wall, resulting in higher CHF values. Higher velocities result in fairly similar interfacial behavior for top wall and bottom wall heating, and double-sided heating exhibiting greater symmetry between interfacial behaviors along the opposite walls. Overall, CHF values for all three configurations converge to one another above 1.5 m/s. This convergence is clearly the result of high inertia negating the influence of gravity. It is shown that interfacial instability theory provides an effective means for assessing the influence of velocity on CHF for top wall versus bottom wall heating. For top wall heating, a stable interface at low velocities causes vapor accumulation against the top wall resulting in very low CHF. Instability theory shows that top wall heating becomes unstable above 1.03 m/s, allowing liquid contact with the wall and improved wall cooling. For bottom wall heating, the interface is always unstable and favorable for liquid contact. Instability theory also shows that inertia dwarfs gravity around 1.5 m/s, where critical wavelengths for top wall and bottom wall heating converge. Convergence of the CHF values for top wall and bottom wall heating also occurred at a similar value.

1. Introduction

1.1. Transitioning from single-phase to two-phase thermal management in future space missions

Subcooled flow boiling is a primary means for thermal management in many applications demanding the dissipation of large heat loads from small surface areas. The merits of flow boiling are derived from reliance on both latent and sensible heat content of a working fluid, which can yield several orders of magnitude enhancement in heat removal compared to single-phase systems. These merits are realized in the nucleate boiling region, provided the heat flux is maintained safely below critical heat flux (CHF). This thermal limit, which is arguably the most important design parameter for a two-phase thermal management system, is associated with interruption of liquid access to the heat dissipating wall, and is known to trigger unsteady escalation in the wall temperature, leading to meltdown, burnout or some other form of catastrophic failure of the heat-dissipating device [1]. This explains the emphasis researchers have placed on determining CHF for a variety of flow boiling configurations, including channel flow [2,3], micro-channel flow [4,5], spray [6,7] and jet [8,9], as well as hybrid micro-channel/jet cooling [10,11].

The merits of subcooled phase change are especially significant for thermal management in space systems, where high two-phase heat transfer coefficients can play a key role in reducing the size and weight of thermal management hardware. In fact, space agencies worldwide are aggressively exploring the implementation of two-phase thermal management to support astronaut life in both space vehicles and planetary bases. The reductions in weight and

* Corresponding author. Tel.: +1 (765) 494 5705; fax: +1 (765) 494 0539.
E-mail address: mudawar@ecn.purdue.edu (I. Mudawar).
URL: https://engineering.purdue.edu/BTPFL (I. Mudawar).

http://dx.doi.org/10.1016/j.ijheatmasstransfer.2015.06.073
0017-9310/

Nomenclature

c_p	specific heat at constant pressure
g	gravity
g_e	Earth gravity
H	height of flow channel's cross-section
h	heat transfer coefficient
$H1$	top heated wall 1
$H2$	bottom heated wall 2
k_c	critical wave number
L_d	development length of flow channel
L_e	exit length of flow channel
L_h	heated length of flow channel
$\dot{m}$	mass flow rate
P	pressure
P_{in}	pressure at inlet to heated portion of channel
q''_w	wall heat flux
T	temperature
t	time
T_{in}	temperature at inlet to heated portion of channel
T_{sat}	saturation temperature
$\Delta T_{sub,in}$	subcooling at inlet to heated portion of channel, $T_{sat} - T_{in}$
T_w	wall temperature
U	mean inlet velocity
W	width of flow channel's cross-section
x_e	thermodynamic equilibrium quality
z	axial coordinate

Greek symbols

δ	mean thickness of liquid or vapor layer
λ_c	critical wavelength
ρ	density
ρ''	modified density
σ	surface tension

Subscripts

avg	average
c	critical
d	developing
e	exit
f	saturated liquid; bulk liquid
g	saturated vapor
h	heated wall
in	inlet to heated portion of channel
n	normal to heated wall; thermocouple location along heated wall
o	outlet from heated portion of channel
sat	saturation
sub	subcooling
w	wall designation ($H1$ or $H2$)

volume amount to appreciable gains in power efficiency. Prime targets for implementation of phase change include Thermal Control Systems (TCSs), which are responsible for controlling the temperature and humidity of the operating environment, and Fission Power Systems (FPSs), which are projected to provide both very high power and very low mass to power ratios [12,13].

But one of the key challenges in adopting phase-change in space applications is limited understanding of the influence of different gravitational environments on two-phase fluid physics and heat transfer, especially on flow boiling CHF.

1.2. Body force effects in flow boiling

Body force can have a strong influence in two-phase flow and heat transfer, especially at low flow velocities. The influence of body force is measured by buoyancy, which is the product of density difference between liquid and vapor, and gravity. Buoyancy influences both vapor removal from the heated wall and liquid replenishment of the wall, thereby impacting both nucleate boiling and CHF.

Many terrestrial two-phase applications capitalize upon the merits of vertical upflow, where buoyancy aids vapor removal from the heated wall in the same direction as the liquid flow. Efficient vapor removal also serves to facilitate liquid replenishment of the wall and enhance both flow stability and CHF. The popularity of vertical upflow explains why the majority of mechanistic models for flow boiling CHF [14–19] are intended for this flow orientation.

However, different applications impose orientations other than vertical upflow. Researchers have attempted to tackle flows in different orientations in pursuit of a mechanistic understanding of the influence of gravity components parallel to the flow and perpendicular to the heated wall on CHF, as well as to develop minimum flow criteria where variations in flow orientation cease to influence CHF, and where the ill effects of certain orientations may be negated.

The horizontal orientation, with gravity perpendicular to the flow direction, is a common flow configuration. Horizontal flow with a bottom heated wall was studied in detail by Zhang et al. [20] for subcooled inlet conditions and Kharangate et al. [21] for saturated inlet conditions. Here, buoyancy aids in vapor removal and liquid replenishment of the heated wall. The opposite is true for horizontal flow with a top heated wall, where buoyancy accumulates the vapor along the heated wall, leading to unusually low CHF values for low velocities [22,23]. Isolating the effects of buoyancy in horizontal flows is achieved with a rectangular channel containing heated walls running parallel to one another. Fig. 1(a) and (b) depict the idealized flow boiling behavior adapted from high speed images for top wall heating and bottom wall heating, respectively. Notice the tendency of vapor for top wall heating, Fig. 1(a), to accumulate into a rather continuous layer, with minimal opportunity for liquid to replenish the heated wall. On the other hand, bottom wall heating, Fig. 1(b), provides greater opportunity for the denser liquid to reach the heated wall, which explains the effectiveness of horizontal flow with bottom wall compared to top wall heating. Fig. 1(c) depicts horizontal two-phase flow in a rectangular channel that is fitted with both top and bottom heating walls. This double-sided heating configuration is far more complex than those depicted in Fig. 1(a) and (b) because the merits of bottom wall heating and detriments of top wall heating are encountered simultaneously in the same flow channel. The benefits or drawbacks of double-sided heating in Earth's gravity are not easily identifiable.

However, double-sided heating was recently examined in microgravity that was simulated by Konishi et al. [24] in parabolic flight experiments. In the absence of gravity for the configuration depicted in Fig. 1(c), equal heat fluxes along the two heated walls produce fairly symmetrical interfacial behavior. With twice the amount of heat supplied to the flow, increased vapor production yielded appreciable acceleration of the flow and a higher CHF compared to one-sided heating in microgravity. However, it is

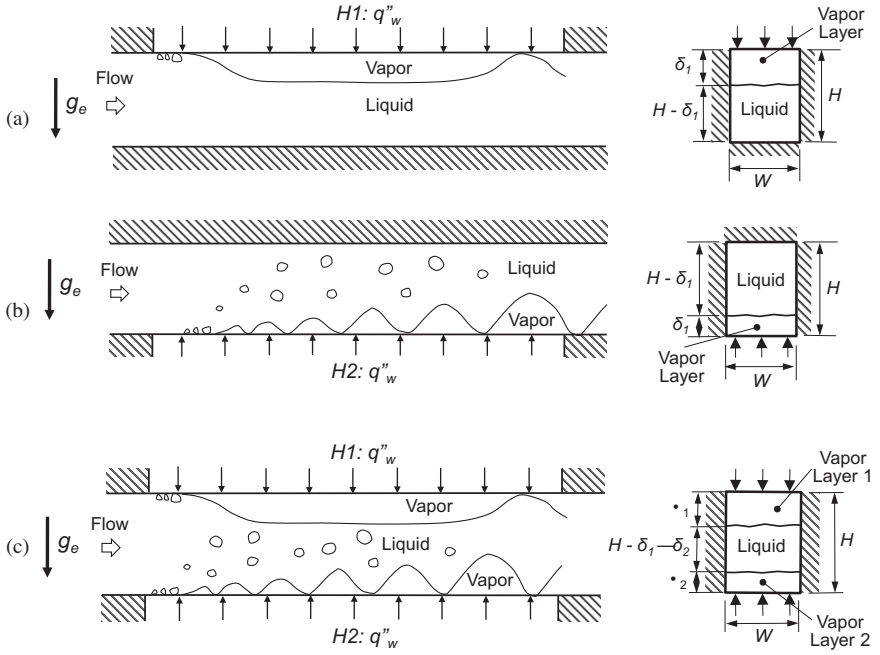

Fig. 1. Depiction of horizontal flow boiling near CHF for a rectangular channel with (a) top wall heating, (b) bottom wall heating, and (c) double-sided heating.

not apparent if double-sided heating can produce similar benefits for horizontal flow in Earth's gravity, given the aforementioned merits of bottom wall heating and detriments of top wall heating.

1.3. Objective of study

The present study will explore interfacial behavior and flow boiling heat transfer up to CHF for horizontal flow corresponding to each of the three heating configurations depicted in Fig. 1(a)–(c). High-speed video imaging is used to better understand the influence of gravity perpendicular to the heated walls on interfacial behavior for the three configurations. Experimental values of both local and spatially averaged heat transfer coefficients, and CHF are also compared for the three configurations.

This study is a part of a NASA project with the ultimate goal of developing the Flow Boiling and Condensation Experiment (FBCE) for the International Space Station (ISS). This study concerns the flow boiling portion of the project, and efforts to determine minimum flow rate criteria for achieving gravity-independent CHF.

2. Experimental methods

2.1. Flow boiling module

Fig. 2(a)–(c) shows the construction of the flow boiling module. This module is comprised of three plates of transparent polycarbonate plastic (Lexan) that are bolted together between two aluminum support plates. The middle Lexan plate is milled to produce a 2.5-mm wide × 5-mm high rectangular flow channel. Rectangular slots are also milled into the top and bottom Lexan plates to accommodate two 15.5-mm wide, 114.6-mm long and 1.04-mm thick oxygen-free copper heating wall slabs. O-ring seals are inserted into shallow grooves in the top and bottom Lexan plates facing the middle Lexan plate for leak prevention. Additional o-rings are inserted into grooves around the perimeter of the copper plates. The flow boiling module assembly is shown in Fig. 2(b). Pressure measurements are made at three positions along the channel, namely, one near the inlet port, one just upstream and one just downstream of the heated copper slabs. Type-E thermocouples are inserted in the middle of the flow channel through the bottom Lexan plate near the inlet and outlet FC-72 ports. Fig. 2(c) shows key axial and cross-sectional dimensions of the flow channel. The channel features a honeycomb flow straightener at the inlet to break any large eddies. An entry length 100 times the hydraulic diameter upstream of the heated portion of the channel ensures fully developed flow.

Fig. 2(d) and (e) shows the detailed construction and instrumentation of the heated walls, respectively. Each heated wall features six 4.5-mm wide and 16.4-mm long thick-film resistors, each with a resistance of 188 Ω, that are soldered to the backside of the copper slab. Powered by a variable voltage source, the six resistors along each wall are connected electrically in parallel to produce a uniform heat flux along the copper slab. As discussed by Zhang et al. [25], the thickness of the copper slab must exceed a minimum threshold value since very small thicknesses restrict axial conduction along the wall and yield CHF values that are wall thickness dependent. For flow boiling of FC-72, Zhang et al. showed that the wall thickness must exceed 0.40 mm to achieve the so-called asymptotic CHF values representative of practical engineering surfaces. A wall thickness of 1.04 mm is therefore used in the present study. Fig. 2(e) shows temperatures of the two walls are measured by two sets of seven Type-E thermocouples that are inserted into shallow holes along the centerline of each copper slab between the resistors. The thermocouples are designated as $T_{wm,n}$, where m represents the heated wall ($H1$ for top heated wall or $H2$ for bottom heated wall), and n the axial thermocouple location. Not shown in Fig. 2(e) is a second set of thermocouples for each copper slab at the same axial locations as the thermocouples used for temperature measurements. The purpose of the second thermocouple set in each copper slab is to cut off power supply to the resistors with the aid of a relay once temperature measured by any thermocouple reaches 130 °C.

2.2. Flow loop

The primary purpose of the flow loop is to deliver the working fluid, FC-72, to the flow boiling module at a prescribed flow rate, pressure, and temperature (or quality). FC-72 is a dielectric liquid

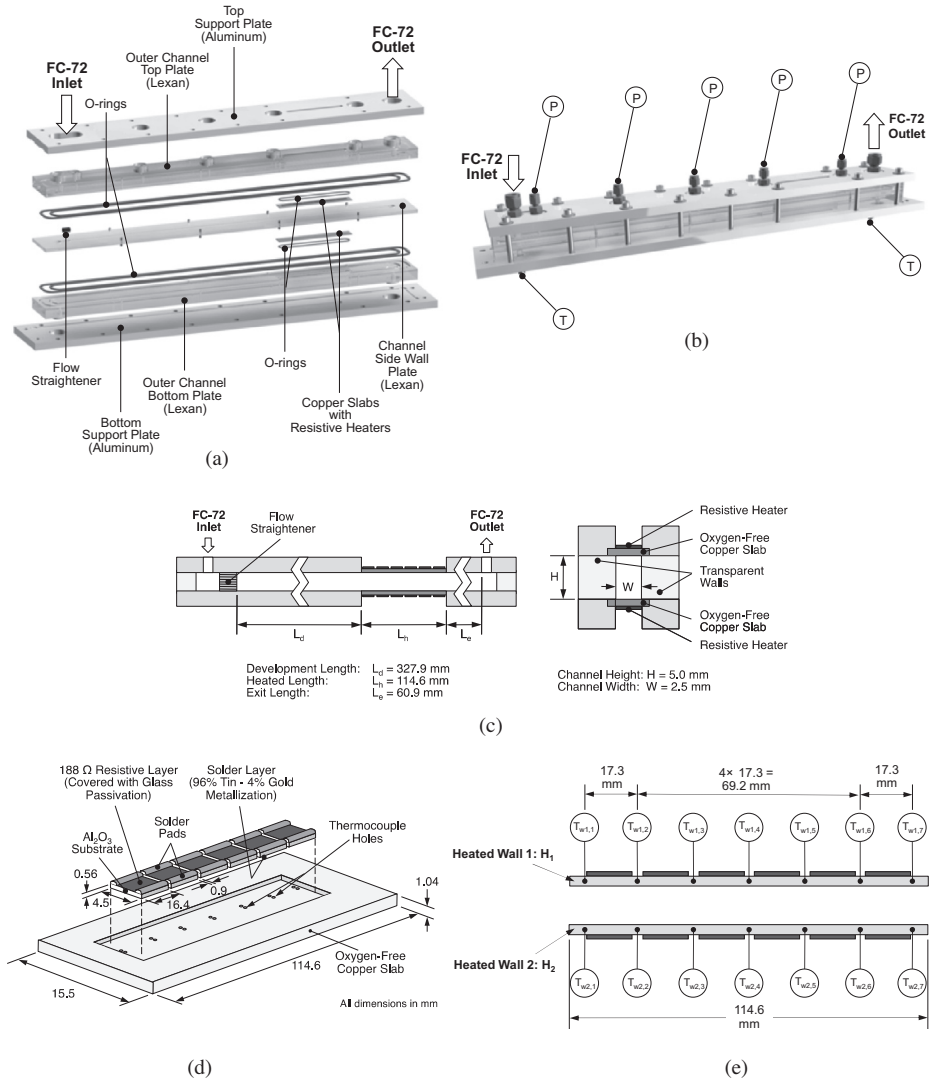

Fig. 2. (a) Exploded view of the flow boiling module. (b) Assembled view of the flow boiling module. (c) Key dimensions of the flow channel. (d) Construction of the heated walls and thick-film resistors. (e) Thermocouple layout in the two heated walls.

with a relatively moderate saturation temperature of T_{sat} = 56 °C at atmospheric pressure. Fig. 3(a) shows a schematic of the flow loop. The system is fitted with a degassing unit that is used to deaerate the test fluid in the flow loop as necessary.

The FC-72 is circulated in the loop with the aid of a variable speed magnetically coupled gear pump. Liquid exiting the pump is passed through a filter, Coriolis flow meter and pre-heater before entering the flow boiling module. Passing through the flow boiling module, the liquid is converted to a two-phase mixture. The mixture continues to a moduler liquid-to-liquid heat exchanger to convert the fluid back to subcooled liquid state. An air-pressurized accumulator is situated between the heat exchanger and pump to help set the lowest pressure (reference pressure point) for the loop and also compensate for any fluid expansion or contraction and phase change throughout the loop.

The entire flow boiling facility, including the flow loop components, data acquisition system, power and instrumentation cabinets, and high-speed camera, are mounted onto a rigid optical table as shown in Fig. 3(b).

2.3. Flow visualization techniques

A high-speed camera is used to capture the two-phase interfacial features along the heated portion of the flow channel. A fixed frame rate of 2002 frames per second (fps) and pixel resolution of 2040 × 156 are used to capture the entire heated length for each test run. Each video image sequence consists of 3000 frames, or 1.50 s of flow visualization data per test run. Illumination is provided from the back of the flow channel by three LEDs, with a light shaping diffuser (LSD) situated between the LEDs and the channel to enhance illumination uniformity.

2.4. Operating conditions and procedure, and measurement uncertainty

The operating conditions for the study are as follows: FC-72 inlet mean liquid velocity of U = 0.11–2.02 m/s, inlet temperature of T_{in} = 53.2–67.3 °C, inlet subcooling of $\Delta T_{sub,in}$ = 1.5–9 °C, and inlet pressure of P_{in} = 99.3–177.1 kPa (14.4–25.7 psi). All test cases are provided in Table 1. The flow loop is first run to achieve steady state conditions at the inlet to the flow boiling module. Once the prescribed inlet conditions are achieved, power is supplied to the flow boiling module's copper wall resistors in small increments, with each increment followed by a waiting period to achieve steady state heated wall temperatures. Over the course of a test run, the mass flow rate is maintained at a constant rate by manually adjusting the pump speed for every heat flux increment. Only after steady state is achieved again, the next heat flux increment is

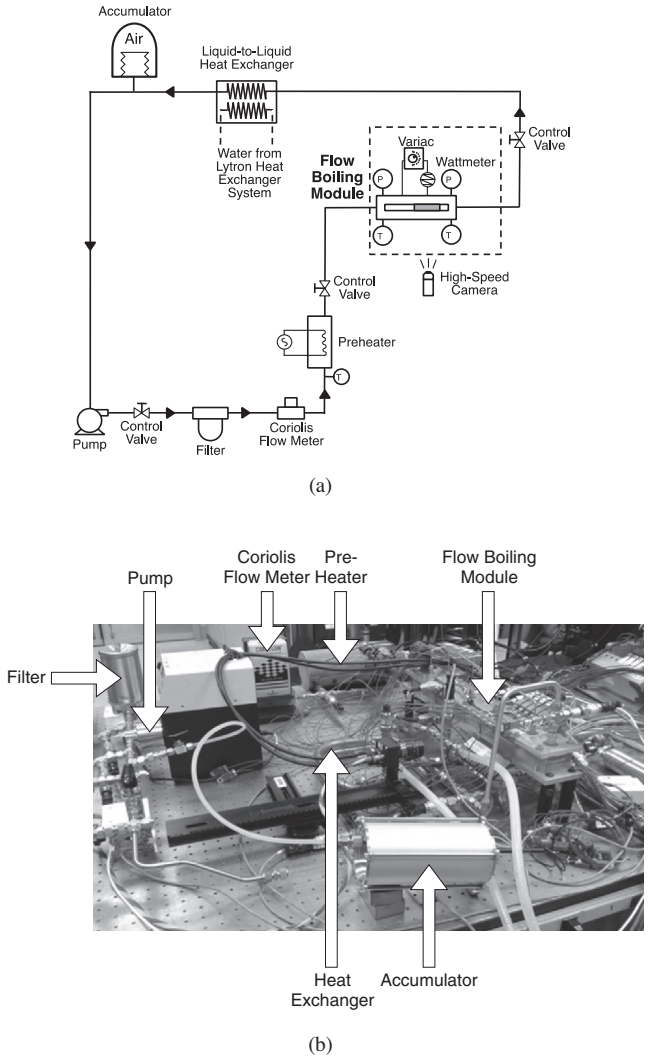

Fig. 3. (a) Schematic diagram of the flow loop. (b) Photo of the test facility.

implemented. The high-speed camera is manually triggered to record data after achieving steady state wall temperatures. A Labview program is used in conjunction with an NI SCXI-1000 data acquisition system to record data throughout the flow boiling facility. Incorporated into the program is a fail-safe feature that automatically cuts off power input to the resistive heaters should any of wall temperatures exceed 130 °C. Aside from protecting the heated walls against burnout, this feature is intended to prevent any breakdown of the FC-72, which may lead to formation of the toxic compound perfluoroisobutene (PFiB).

Fluid and wall temperatures throughout the flow boiling facility are measured with type-E thermocouples having an accuracy of ±0.5 °C. STS absolute pressure transducers having an accuracy of ±0.05% are used to measure pressures at several locations along the flow boiling module and the flow loop. The Coriolis flow meter has an accuracy of ±0.1%.

3. Flow visualization results

Fig. 4(a)–(f) shows individual images of flow boiling along the entire heated portion of the channel for top wall heating, top and bottom wall heating, and bottom wall heating at mean inlet velocities of $U = 0.11–2.02$ m/s and heat fluxes up to CHF, with subcoolings at the inlet to the heated portion ranging from 1.9 to 8.4 °C. A dominant feature clearly visible in all the images is formation of a wavy vapor layer along the heated walls. Notice that the vapor–liquid interface of this layer makes occasional contact with the wall such that the wall is covered mostly with vapor and to a lesser extent with liquid. Because of the poor thermophysical properties of vapor, cooling of the heated wall is provided mostly by the moving liquid-wall contact regions – wetting fronts.

In this study, the top wall of the rectangular channel is designated as $H1$ and bottom wall as $H2$. For the lowest velocity of $U = 0.11–0.13$ m/s, Fig. 4(a) depicts strong gravitational effects for all three heating configurations. For top wall heating, with only heater $H1$ on, the vapor generated along $H1$ remains in contact $H1$, and is stratified above the liquid. Increasing the heat flux for top wall heating increases the amount of vapor generated, which in turn, decreases the wetting front area of liquid contact with $H1$. CHF is observed to occur as the wetting front area decreases appreciably and the vapor covers the majority of the heated wall. For the bottom heated wall configuration, with only heater $H2$ on, strong gravitational effects are manifest by the vapor generated at the bottom wall easily crossing over to the top wall before being convected downstream by the liquid. As the vapor departs from the heated wall, the incoming liquid quickly occupies the spaces vacated by the escaping vapor. This behavior bears some resemblance to pool boiling, but with the added advantage of slow moving incoming flow assisting the liquid replenishment. CHF occurs when the bottom wall is completely covered with a thick vapor layer, with a high rate of vapor production hindering any liquid access to $H2$. The third configuration involves double-sided heating with heaters $H1$ and $H2$ simultaneously turned on. Here,

Table 1
Test cases for study.

Test case	Accumulator pressure (kPa)	Heated wall	U (m/s)	T_{in} (°C)	P_{in} (kPa)	CHF (W/cm^2)
1	101.33	Top	0.13	53.2	99.3	6.3
2	101.33	Top	0.24	55.7	103.4	9.3
3	101.33	Top	0.49	54.4	105.1	16.3
4	101.33	Top	0.99	53.6	107.9	23.1
5	101.33	Top	1.50	55.1	114.3	27.4
6	101.33	Top	1.99	58.7	130.8	31.0
7	101.33	Bottom	0.11	54.4	103.3	24.9
8	101.33	Bottom	0.25	55.3	104.6	27.1
9	101.33	Bottom	0.49	54.5	106.5	27.1
10	101.33	Bottom	0.99	53.8	110.0	29.4
11	101.33	Bottom	1.49	55.2	114.9	29.4
12	101.33	Bottom	1.99	58.5	130.5	31.8
13	101.33	Top & Bottom	0.11	54.6	102.8	8.6
14	101.33	Top & Bottom	0.24	55.7	105.6	18.0
15	101.33	Top & Bottom	0.49	54.9	111.0	25.0
16	101.33	Top & Bottom	0.99	54.6	118.4	29.6
17	101.33	Top & Bottom	1.49	55.9	126.2	32.0
18	101.33	Top & Bottom	2.02	59.5	145.1	33.2
19	122.04	Top	0.13	56.4	119.7	6.9
20	122.04	Top	0.25	58.9	122.0	9.3
21	122.04	Top	0.50	60.1	127.5	17.2
22	122.04	Top	0.75	60.5	133.3	21.0
23	122.04	Top	0.98	62.6	136.3	23.1
24	122.04	Top	2.02	67.2	161.5	31.0
25	122.04	Bottom	0.13	56.8	130.1	27.1
26	122.04	Bottom	0.25	59.1	128.7	28.2
27	122.04	Bottom	0.50	60.6	130.5	29.4
28	122.04	Bottom	0.75	60.5	136.0	28.2
29	122.04	Bottom	0.98	62.5	137.6	28.2
30	122.04	Bottom	2.02	66.9	161.8	31.8
31	122.04	Top & Bottom	0.13	57.7	128.4	8.6
32	122.04	Top & Bottom	0.25	59.5	129.7	18.0
33	122.04	Top & Bottom	0.50	60.2	134.2	25.0
34	122.04	Top & Bottom	0.75	61.5	144.6	28.4
35	122.04	Top & Bottom	0.97	64.0	150.2	29.6
36	122.04	Top & Bottom	1.52	64.7	162.1	32.0
37	122.04	Top & Bottom	2.04	67.7	177.1	33.2

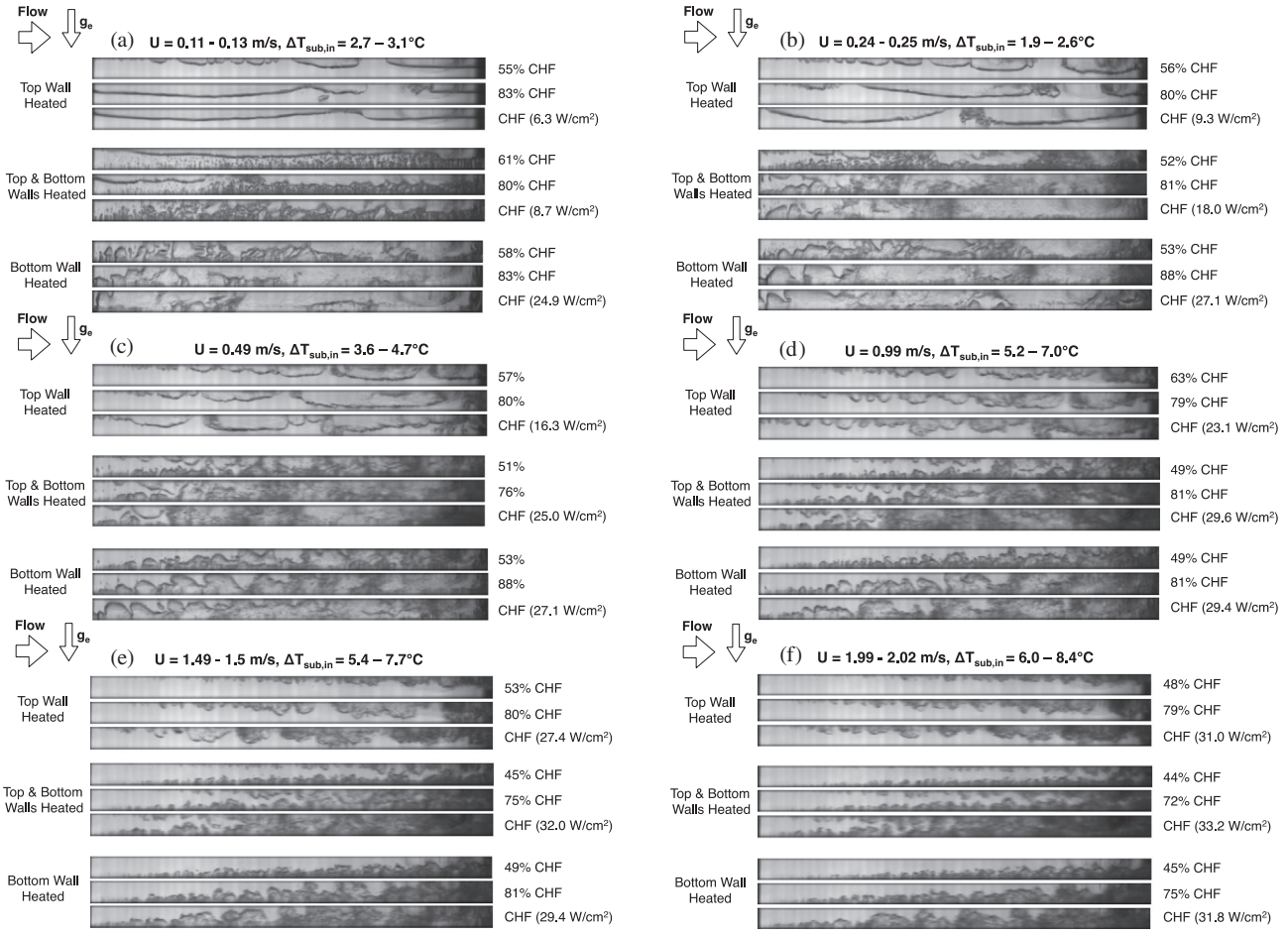

Fig. 4. Variations of interfacial behavior with increasing heat flux for top wall heating, double-sided heating, and bottom wall heating for (a) U = 0.11–0.13 m/s, (b) U = 0.24–0.25 m/s, (c) U = 0.49 m/s, (d) U = 0.99 m/s, (e) U = 1.49–1.5 m/s, and (f) U = 1.99–2.02 m/s.

interfacial behavior appears to combine interfacial behaviors associated with either $H1$ or $H2$ individually turned on. The vapor generated along the top wall remains in contact with the top wall, while the vapor generated from the bottom wall crosses over towards the top wall. For the low velocity of U = 0.11–0.13 m/s, gravity appears to stabilize the vapor layer along the top heated wall, with vapor residing above liquid, which also hinders wetting front formation along $H1$. On the other hand, gravity plays a destabilizing role on the vapor layer along the lower heated wall, with liquid residing above vapor. This destabilizing effect serves to promote liquid access to the same wall along $H2$.

For the next velocity of U = 0.24–0.25 m/s, Fig. 4(b) depicts behavior similar to that for U = 0.11–0.13 m/s, but with increasing inertia effects. The most obvious differences between the two velocities for top wall heating are shorter wavelength and increased number of wetting fronts for the higher velocity. Fig. 4(c) and (d) shows interfacial behavior as the velocity is increased to 0.49 and 0.99 m/s, respectively. The images depicted in these figures display a further decrease in wavelength and increase in number of wetting fronts for the top wall heating. They also show the vapor produced along the bottom wall for bottom wall heating incurs appreciable difficulty crossing to the top wall, and results in a wavy vapor layer along the lower wall. But the most important observations for 0.49 and 0.99 m/s concern double-sided heating, where somewhat similar vapor layers are observed along the opposite heated walls. This observation is crucial in defining a shift between gravity-dominated and inertia-dominated flows. The flow becomes even more inertia dominated for U = 1.49–1.5 m/s, Fig. 4(e), and U = 1.99–2.02 m/s, Fig. 4(f), evidenced by better symmetry in boiling behavior along the opposite walls for double-sided heating. It is interesting to note that the same symmetry was captured by Konishi et al. [24] for U = 0.1–1.9 m/s for double-sided heating in the microgravity environment of parabolic flight.

Fig. 5 shows 15 sequential images spaced 1.4 ms apart for top wall heating, with only $H1$ on, for U = 0.13–1.99 m/s and 79–83% CHF. At U = 0.13 m/s, some nucleation is observed near the leading edge of the heated wall, and the vapor quickly coalesces into a wavy vapor layer that propagates downstream. For this low velocity, most of the heated wall is covered with vapor. Increasing the flow velocity causes the nucleation commencement to move downstream, and the wavy vapor layer's average wavelength to decrease, allowing for creation of an increasing number of wetting fronts.

Fig. 6 shows 15 sequential images spaced 1.4 ms apart for bottom wall heating, with only $H2$ turned on, for U = 0.11–1.99 m/s and 75–88% CHF. At U = 0.12 m/s, gravity serves to increase the thickness of the vapor layer generated along the bottom heated wall. The wavy vapor layer becomes more clearly discernable at higher velocities. Nucleation is shown commencing farther upstream for bottom wall heating compared to the top wall heating configuration depicted in Fig. 5. This is attributed to gravity aiding in both vapor removal from the bottom wall as well as liquid replenishment. Fig. 6 shows velocities at or above 0.49 m/s are

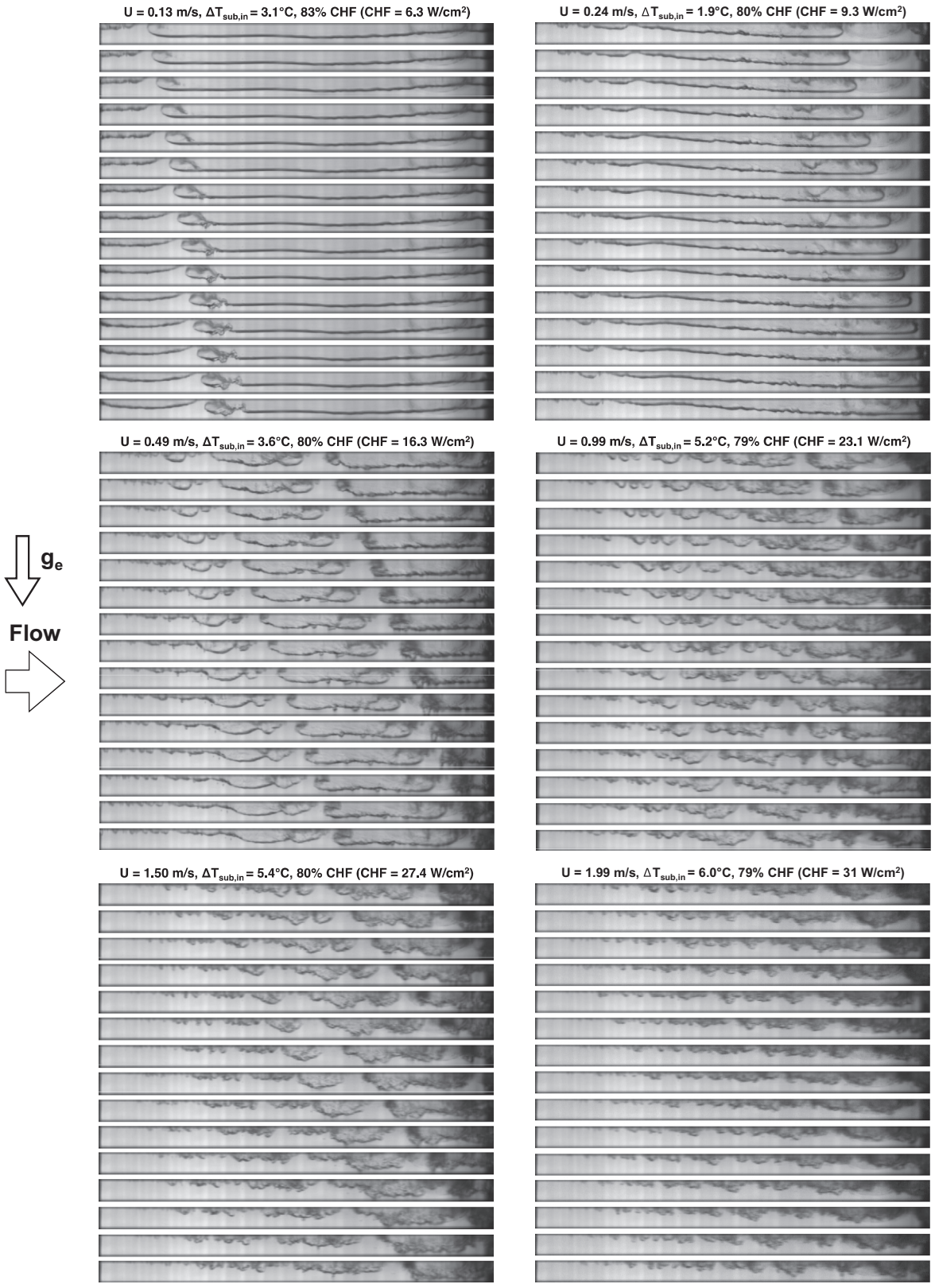

Fig. 5. Sequential high-speed video images from top wall heating experiments for different inlet velocities.

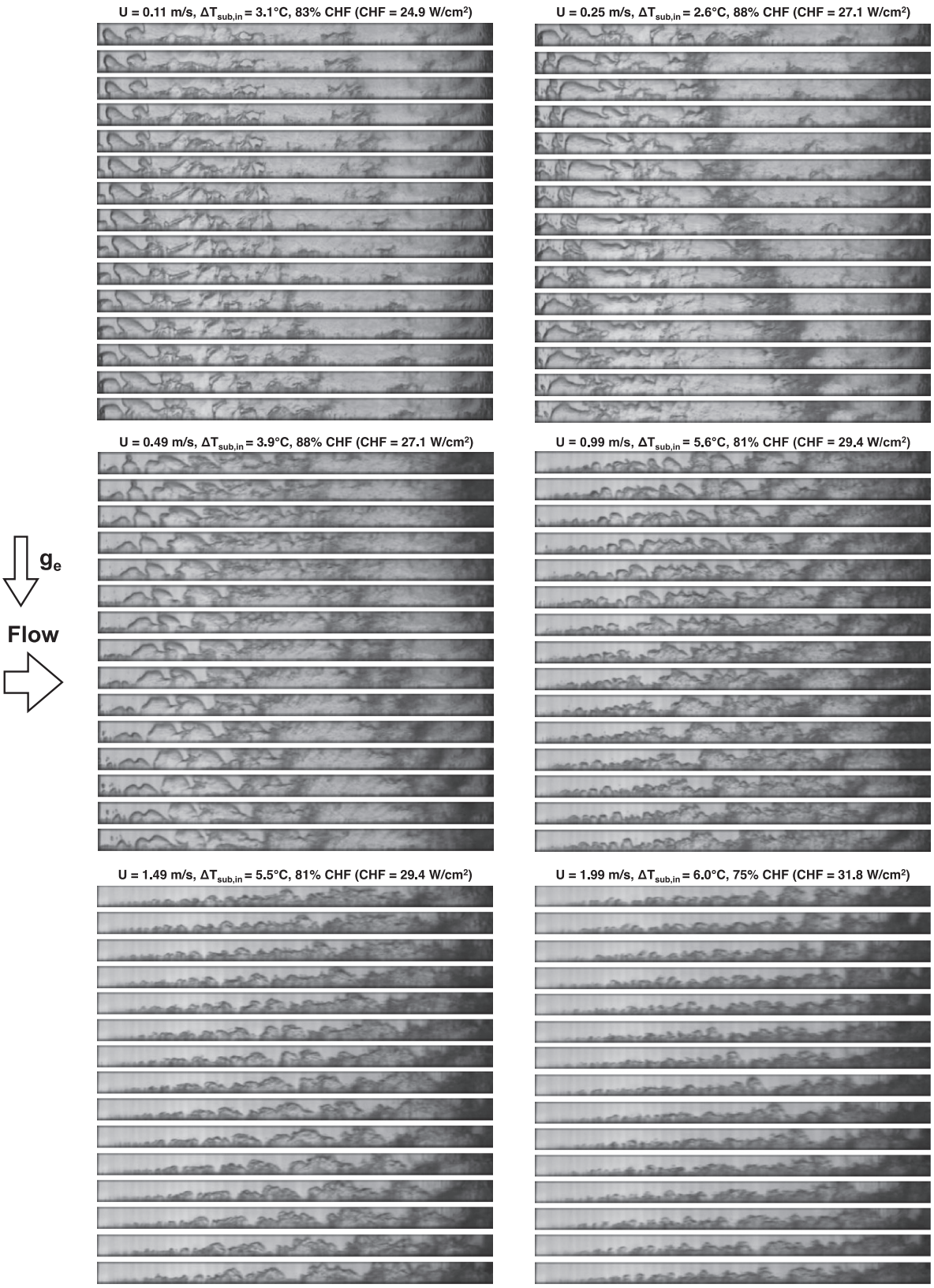

Fig. 6. Sequential high-speed video images from bottom wall heating experiments for different inlet velocities.

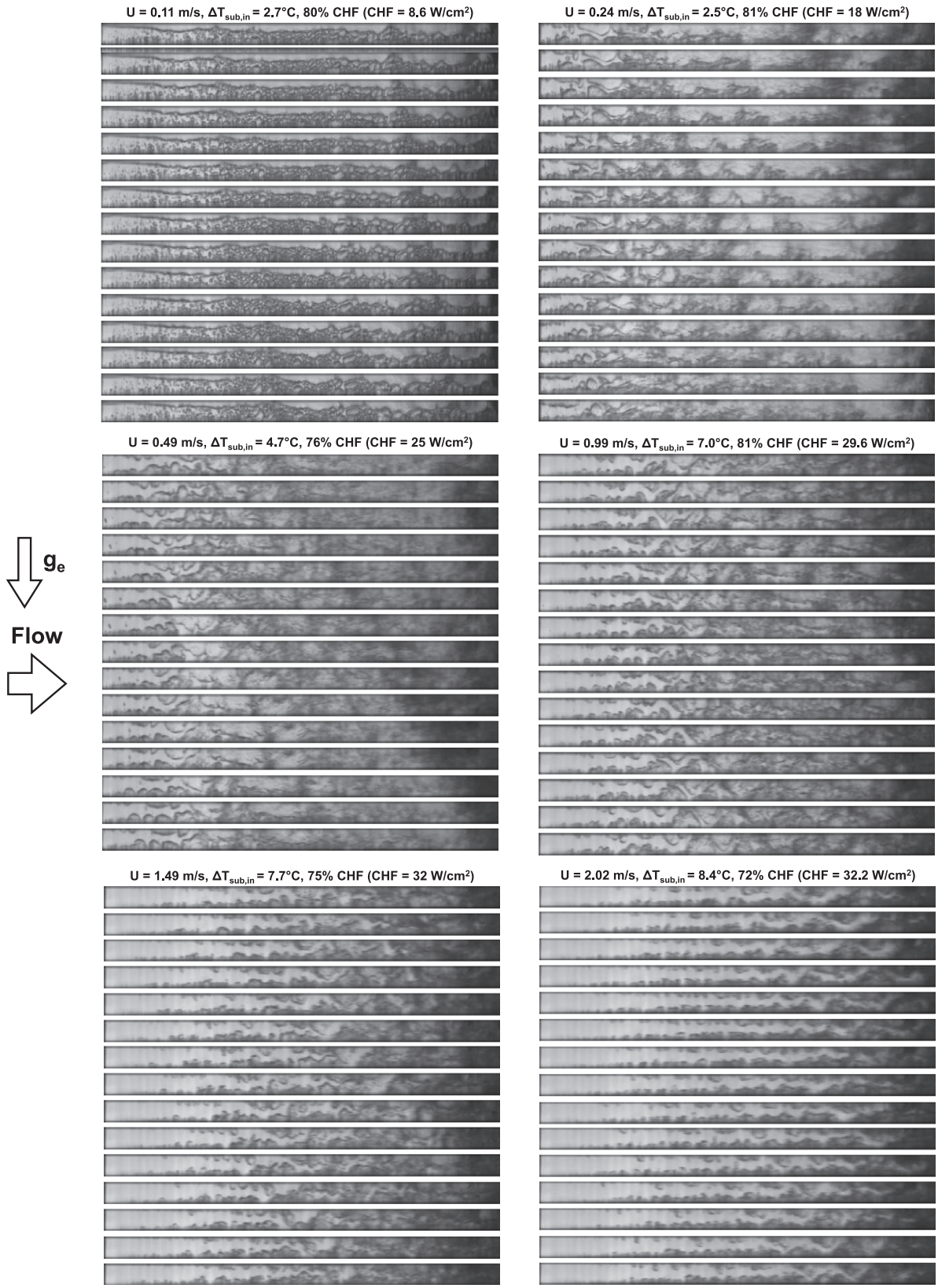

Fig. 7. Sequential high-speed video images from double-sided heating experiments for different inlet velocities.

associated with a more clearly defined wavy vapor layer and wetting fronts along the heated wall.

Fig. 7 shows 15 sequential images spaced 1.4 ms apart for double-sided heating, with $H1$ and $H2$ simultaneously turned on, for U = 0.13–2.02 m/s and 72–81% CHF. This configuration combines the effects of the other two heating configurations discussed in conjunction with Figs. 5 and 6. For U = 0.13 m/s, gravity has an appreciable influence on boiling behavior, evidenced by marked differences between vapor layer formations along the top and bottom heated walls. Better symmetry is achieved at higher

velocities, indicating a weakening influence of gravity compared to inertia. Despite this overall symmetry, the vapor layers exhibit a wavy 'meshing' behavior, where the wave peak from one of the heated walls grows towards the trough (wetting front) between two wave peaks on the opposite wall, similar to meshing of gears. This is similar to the wavy meshing behavior observed by Konishi et al. [24] for $U = 0.1–1.9$ m/s in microgravity.

All flow visualization results discussed thus far concern fluxes presented as a percentage of CHF for a given velocity and heating configuration. On the other hand, Fig. 8 shows interfacial behavior for the three heating configurations for equal wall heat fluxes. For $U = 0.11–0.13$ m/s and $q''_w = 5.3$ W/cm^2, there are drastic differences in interfacial behavior along $H1$ and $H2$. For top wall heating, vapor stratifies into a fairly continuous vapor layer along $H1$. For bottom wall heating, vapor is generated along $H2$ and accumulates in the axial direction while rising towards $H1$. For $U = 0.11–0.13$ m/s and $q''_w = 5.3$ W/cm^2, double-sided heating seems to combine the interfacial behaviors of top wall and bottom wall heating. For $U = 0.99–2.02$ m/s, double-sided heating exhibits somewhat similar interfacial behavior along both walls as high inertia appears to be increasingly effective at negating gravity effects.

4. Experimental results

4.1. CHF results

Fig. 9(a) and (b) shows the variation of CHF with mean inlet velocity for top wall heating, bottom wall heating, and double-sided heating, with the accumulator set to atmospheric pressure and to 122.04 kPa, respectively. Both figures show CHF for all velocities is lowest for top sided heating, with only $H1$ turned on. This behavior is attributed to buoyancy aiding the accumulation of vapor along the top heated wall, while resisting liquid access to the same wall. Notice how CHF is vanishingly small for the lowest velocity of $U = 0.11$ m/s, where stratification is strongest and inertia weakest. As shown in Fig. 5, increasing velocity for top wall heating decreases the wavelength of the vapor layer, enabling better liquid access to the heated wall, which is manifest in Fig. 9(a) and (b) by CHF increasing appreciably with increasing velocity.

For bottom wall heating, with only $H2$ turned on, CHF is appreciably higher than that for top wall heating for the lowest velocity. This can be explained by buoyancy aiding the removal of vapor bubbles and promoting better liquid access for bottom wall heating. When compared to top wall heating, CHF is seen to be relatively insensitive to velocity.

For double-sided heating, CHF for the lowest velocity of $U = 0.11$ m/s is close to that for top wall heating. This is because both heated walls are turned off once CHF is encountered in either wall, and because CHF occurs much earlier along the top wall. For the same reason, CHF for double-sided heating increases at about the same rate as that for top wall heating for $U = 0.1–0.99$ m/s. However, double-sided heating offers a key advantage over top wall heating, which stems from greater acceleration of the flow due to vapor generation along both walls simultaneously. This advantage is exhibited by higher CHF compared to top wall heating for the entire velocity range, as well as a higher CHF for double-sided heating compared to even bottom wall heating for $U \geqslant 0.99$ m/s. Overall, CHF values for all three heating configurations converge to one another with increasing velocity. This convergence is clearly associated with increased flow inertia and gradual negation of gravity influences.

4.2. Flow boiling curves

As discussed earlier each heated wall is fitted with seven thermocouples for wall temperature measurement. The temperatures are designated as $T_{w1,n}$ and $T_{w2,n}$, where *1* and *2* refer to heated walls $H1$ and $H2$, respectively, and n thermocouple axial location along the heated wall as shown in Fig. 2(e). Fig. 10(a)–(c) shows boiling curves for $U = 0.24–2.02$ m/s for top wall heating, bottom wall heating, and double-sided heating, respectively. The wall heat flux, q''_w, is plotted against the difference between average wall temperature, $T_{w,avg}$, and inlet saturation temperature, $T_{sat,in}$. All

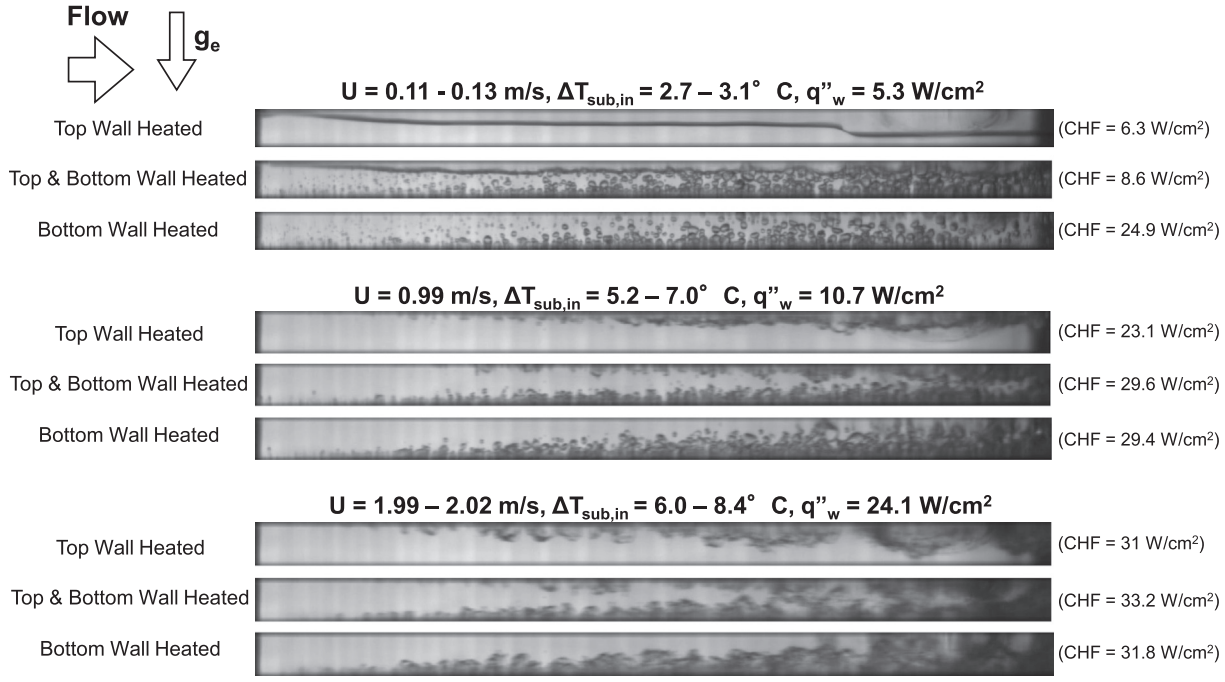

Fig. 8. Comparison of interfacial behavior from top wall heating, double-sided heating and bottom wall heating experiments at equal wall heat fluxes for $U = 0.11–0.13$ m/s, 0.99 m/s, and 1.99–2.02 m/s.

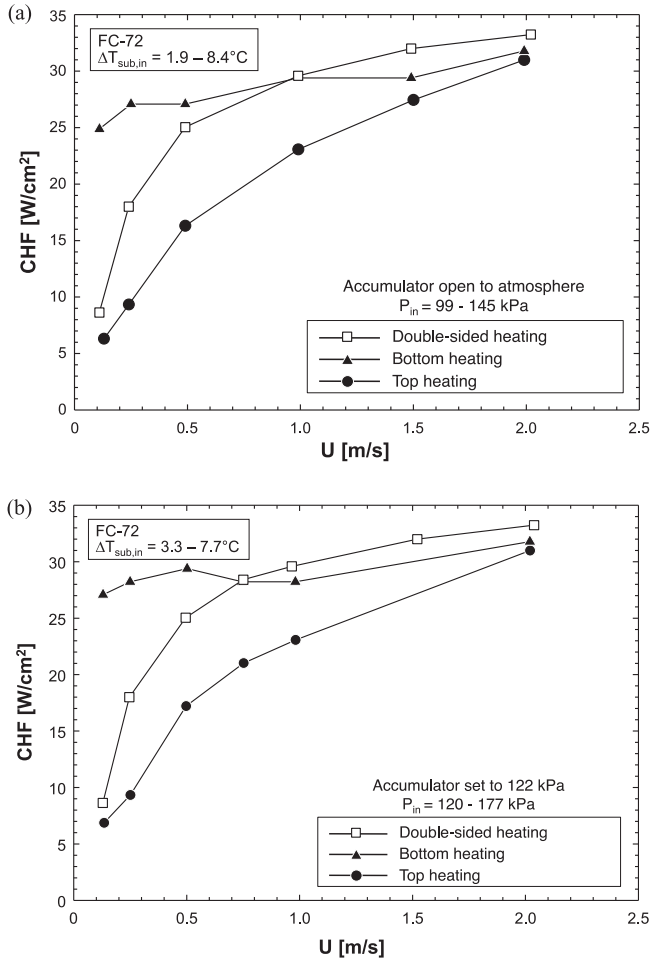

Fig. 9. Variation of CHF with mean inlet velocity for top wall heating, bottom wall heating and double-sided heating with (a) accumulator open to atmosphere, and (b) accumulator set to 122.04 kPa.

curves exhibit the expected boiling curve trends, with the slope increasing sharply upon transitioning from single-phase heat transfer to nucleate boiling, and degrading appreciably as CHF is approached. Both top wall heating, Fig. 10(a), and double-sided heating, Fig. 10(c), exhibit the profound influence of velocity on CHF as discussed in the previous section. Notice that Fig. 10(c) shows individual boiling curves for double-sided heating, and CHF commences along the top heated wall for $U = 0.24$ and 0.99 m/s, and the bottom heated wall for $U = 2.02$ m/s. Additionally, the slope for double-sided heating in the nucleate boiling region is much steeper for $U = 2.02$ m/s than for the other two heating configurations. These trends reflect the aforementioned advantages of greater flow acceleration for double-sided heating.

4.3. Wall temperatures

Fig. 11(a)–(c) shows temporal records of the heated wall temperatures for top wall heating, bottom wall heating, and double-sided heating during the CHF transient for $U = 0.24$–0.25, 0.99, and 1.99–2.02 m/s, respectively. The x-axis in these plots shows the time in seconds starting from the instant the last heat flux increment that culminated in CHF is initiated. As indicated earlier, the power to the heaters is automatically cut off once any of the relay thermocouples exceeds 130 °C. For $U = 0.24$–0.25 m/s, Fig. 11(a) shows top wall heating associated with a slow wall temperature transient response compared to bottom wall heating. This difference in response time can be related to the much smaller heat input for the top wall heating (CHF = 9.3 W/cm^2) compared to bottom wall heating (CHF = 27.1 W/cm^2). For double-sided heating at the same low velocity, CHF is dictated mostly by the thermal response of the top wall. For $U = 0.99$ m/s, Fig. 11(b) also shows a slower response for top wall heating compared to bottom wall heating, but with differences in response time much smaller than for $U = 0.24$–0.25 m/s. Also for $U = 0.99$ m/s, Fig. 11(b) shows both walls for double-sided heating undergoing temperature excursions simultaneously at CHF. For $U = 1.99$–2.02 m/s, where CHF values are fairly similar for the three configurations (31.0, 31.8 and 33.2 W/m^2 for top wall heating, bottom wall heating and double-sided heating, respectively), the temperature response is rapid but fairly similar for all three heating configurations.

Fig. 11(a)–(c) also point to systematic trends concerning the axial location where CHF is first detected. For $U = 0.24$–0.25 m/s, Fig. 11(a) shows temperatures for the three heating configurations increase from the leading edge of the heated wall (T_{w1}) to a maximum immediately downstream from the middle (T_{w5} or T_{w6}), before decreasing again towards the exit (T_{w7}). As discussed later, the downstream decrease in wall temperature is attributed mostly to fluid acceleration along the channel resulting from vapor accumulation. For $U = 0.99$ m/s and 1.99–2.02 m/s, Fig. 11(b) and (c), shows, respectively, a fairly similar sequence of temperature variations for all three configurations as for $U = 0.24$–0.25 m/s but with shorter and closer response times.

4.4. Heat transfer coefficient

The local heat transfer coefficient at a thermocouple location along a heated wall is obtained from the relation

$$h_{m,n} = \frac{q''_w}{(T_{wm,n} - T_f)}, \tag{1}$$

where q''_w is the wall heat flux, $T_{wm,n}$ the wall temperature measured along heated wall m ($m = 1$ for $H1$ and 2 for $H2$), n the thermocouple location, and T_f the bulk fluid temperature. In this study, liquid enters the heated portion of the channel slightly subcooled and is heated up to T_{sat} before bubbles can begin to nucleate. For double-sided heating, the bulk fluid temperatures for the subcooled and saturated regions are given, respectively, by

$$T_{f,n+1} = T_{f,n} + \frac{(q''_{w1} + q''_{w2})\, W \Delta z}{\dot{m} c_{p,f}} \quad \text{for} \quad x_e < 0 \tag{2a}$$

and

$$T_f = T_{sat} \quad \text{for} \quad 0 \leqslant x_e \leqslant 1. \tag{2b}$$

The above equations are also used for single-sided heating by setting $q''_{w1} = 0$ for bottom wall heating, or $q''_{w2} = 0$ for top wall heating. A single value of the heat transfer coefficient is determined for each thermocouple location, and the values are then spatially averaged to determine h_{avg}.

Fig. 12(a)–(c) shows the variations of h_{avg} with wall heat flux for $U = 0.24$–2.02 m/s for top wall heating, bottom wall heating, and double-sided heating, respectively. A general trend for all three configurations is an initial increase in h_{avg} with increasing heat flux towards a peak value before degrading towards CHF. This behavior is clearly reflected in the boiling curves shown in Fig. 10(a)–(c). With top wall heating, with only $H1$ turned on, Fig. 12(a) shows peak h_{avg} value increasing monotonically with increasing velocity. For bottom wall heating, with only $H2$ turned on, Fig. 12(b) shows a weaker variation of peak h_{avg} with increasing velocity. For double-sided heating, Fig. 12(c) shows trends that more or less

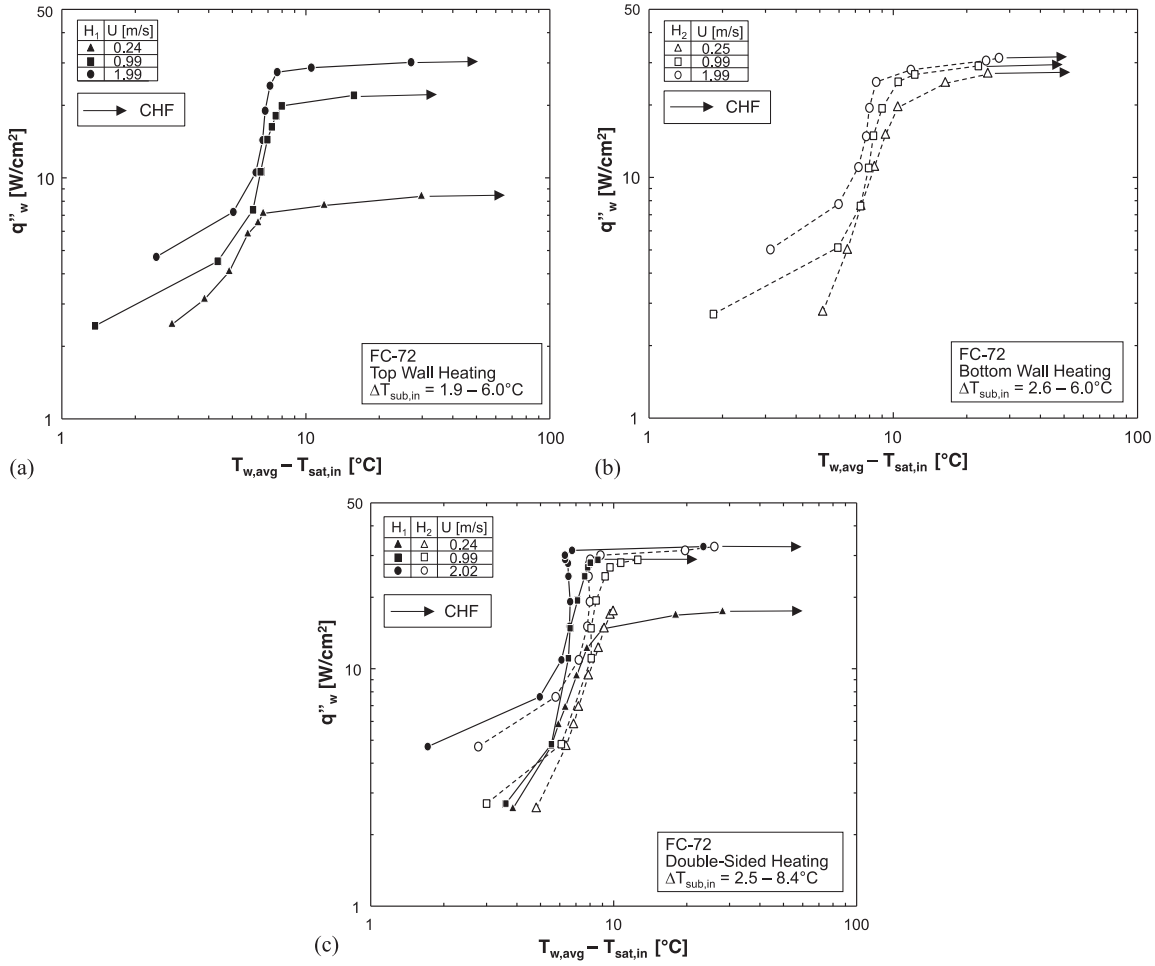

Fig. 10. Boiling curves for different inlet velocities for (a) top wall heating, (b) bottom wall heating, and (c) double-sided heating.

combine those of the individually heated walls, with the highest velocity yielding the highest peak h_{avg} values.

Fig. 13(a)–(c) shows variations of the local heat transfer coefficient along the heated length with increasing heat flux for U = 1.99–2.02 m/s and top wall heating, bottom wall heating, and double-sided heating, respectively. For all three heating configurations, h generally decreases in the flow direction in the upstream region of the heated portion of the channel before increasing again in the downstream region. The relatively high h values near $z = 0$ can be explained by initiation of a thermal boundary layer in the liquid for low heat fluxes, and discrete bubble nucleation at higher fluxes. The degradation in about the upstream half of the heated length is attributed to vapor bubble coalescence to large vapor patches that partially insulate the heated wall. The downstream enhancement in h is the result of fluid acceleration due to increased vapor void. Notice how the downstream enhancement is most pronounced for double-sided heating, Fig. 13(c), where vapor accumulation is highest.

All three heating configurations exhibit a vastly different trend of h versus z for heat fluxes just preceding CHF. For top wall heating, Fig. 13(a) shows h increasing with increasing heat flux up to 76% CHF. At 89% CHF, h begins to display some degradation around the middle of the heated region, which suggests significant vapor buildup in this region begins to offset the influence of flow acceleration. This degradation is intensified for 92% CHF and moves farther upstream. At 96% CHF, the degradation is even more pronounced and felt starting at $z = 0$. Similar trends are observed with bottom wall heating, Fig. 13(b), and double-sided heating, Fig. 13(c).

Fig. 14(a)–(c) shows the variations of h along the heated length for different velocities for top wall heating, bottom wall heating, and double-sided heating, respectively. The values of wall heat flux in these figures correspond to those that yielded peak h_{avg} values in Fig. 12(a)–(c). For top wall heating, Fig. 14(a) shows increasing U improves the peak heat transfer performance. This can be explained by the lower velocities resulting in formation of a broad continuous vapor layer along the heated wall, Fig. 5, and the higher velocities aiding breakup of the vapor layer and increasing the number of wetting fronts. However, Fig. 14(b) shows the influence of velocity is relatively insignificant for bottom wall heating because, as discussed earlier, this orientation facilitates vapor removal by buoyancy and liquid replenishment for all velocities. Comparing all three heating configurations shows double-sided heating, Fig. 14(c), yields the best heat transfer performance. This superior performance can be attributed to two reasons. First, heating along both walls greatly increases vapor production and therefore acceleration of the flow, especially downstream. Second, interaction between the opposite vapor layers appears to enhance mixing and turbulence and, therefore, heat transfer performance. Interestingly, Fig. 14(c) shows the peak heat transfer performance is better for U = 0.99 m/s compared to U = 2.02 m/s. This unexpected trend may be related to the relationship between vapor production and flow acceleration for these conditions. For the same heat flux, the lower velocity yields higher vapor void, especially

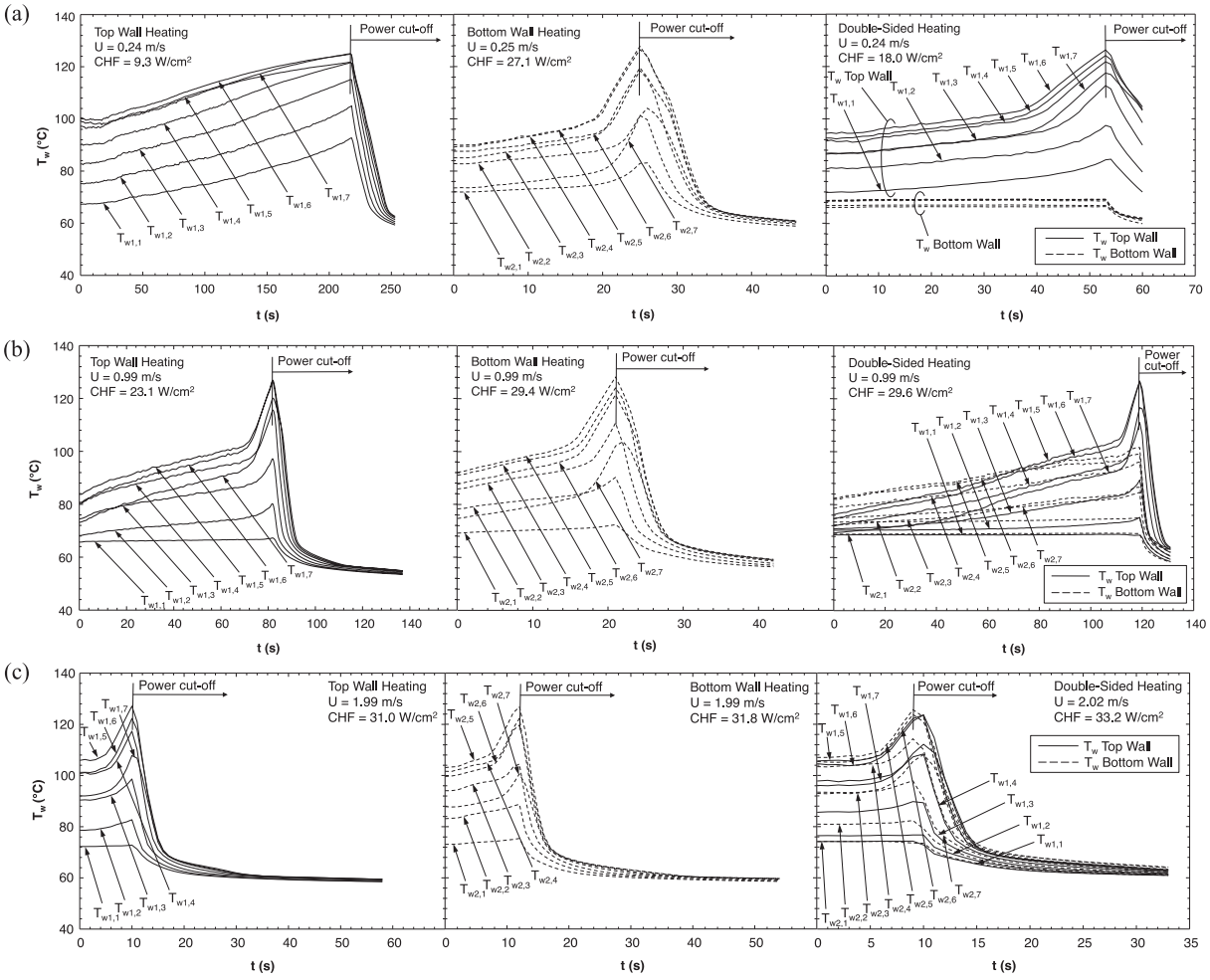

Fig. 11. Temporal records of wall thermocouples during CHF transient for top wall heating, bottom wall heating and double-sided heating for (a) U = 0.24–0.25 m/s, (b) U = 0.99 m/s, and (c) U = 1.99–2.02 m/s.

downstream, and offsets the benefits of higher inlet velocity. This implies that, for the same heat flux, an optimal intermediate velocity may exist where heat transfer performance is more advantageous. However, this same velocity will not yield a higher CHF, since CHF increases monotonically with increasing U as shown in Fig. 9(c). Hence, one must decide if heat transfer or CHF are most important for a given horizontal double-sided heating application.

4.5. Gravity influence on interfacial wavelength

Konishi et al. [26] described how formation of the wetting fronts responsible for cooling of the heated wall prior to CHF relies on interfacial instability of the wavy vapor layer adjacent to the heated wall. For an unstable interface, the critical wavelength, λ_c, is derived from the critical wave number, k_c, which is given by

$$k_c = \frac{2\pi}{\lambda_c} = \frac{\rho_f'' \rho_g'' (U_g - U_f)^2}{2\sigma(\rho_f'' + \rho_g'')} + \sqrt{\left[\frac{\rho_f'' \rho_g'' (U_g - U_f)^2}{2\sigma(\rho_f'' + \rho_g'')}\right]^2 + \frac{(\rho_f - \rho_g) g_n}{\sigma}}, \quad (3)$$

where ρ_f'', ρ_g'', U_g, U_f and g_n are the modified vapor density, modified liquid density, mean velocity of the wavy vapor layer, mean velocity of the surrounding liquid layer, and component of gravity normal to the heated wall. For the top heated wall $H1$ and bottom heated wall $H2$, g_n is given, respectively, by

$$g_{n,1} = -g_e \quad (4a)$$

and

$$g_{n,2} = g_e. \quad (4b)$$

As discussed by Konishi et al., the modified vapor and liquid density terms are influenced by the thicknesses of the vapor and liquid layers, respectively. A simplified analysis of the influence of g_n on critical wavelength for top heated and bottom heated walls can achieved by setting $\rho_g'' = \rho_g$ and $\rho_f'' = \rho_f$ in Eq. (3).

Fig. 15 shows the variation of the critical wavelength, λ_c, for top wall heating and bottom wall heating with velocity difference $\Delta U = U_g - U_f$, with all fluid properties based on a saturation pressure of 150 kPa. It should be noted that the wavy interface is unstable and Eq. (3) is therefore valid only when the expression under the radical is positive, otherwise the interface is stable where the same expression is negative. A negative expression is possible for top wall heating where $g_{n,1} = -g_e$ and small ΔU. Fig. 15 shows top wall heating yields a stable interface for $\Delta U < 1.03$ m/s. In the stable region, top wall heating yields a stable stratified vapor layer adjacent to the heated wall, with no opportunity to form wetting fronts. This explains the very low CHF values for this heating configuration at low velocities. For $\Delta U > 1.03$ m/s, the critical wavelength decreases monotonically from very large values with increasing ΔU. On the other hand, bottom wall heating always yields an unstable interface, with the critical wavelength

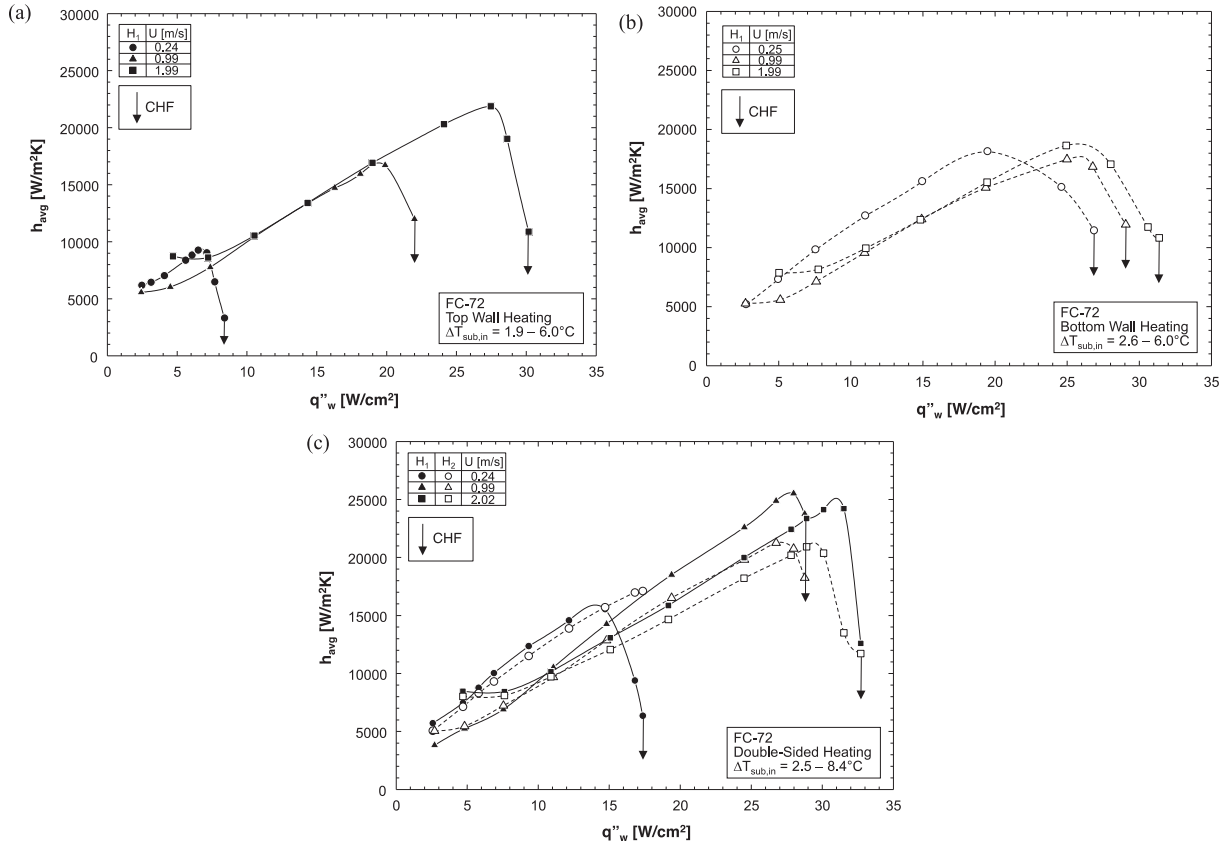

Fig. 12. Variation of average heat transfer coefficient with wall heat flux for different inlet velocities for (a) top wall heating, (b) bottom wall heating, and (c) double-sided heating.

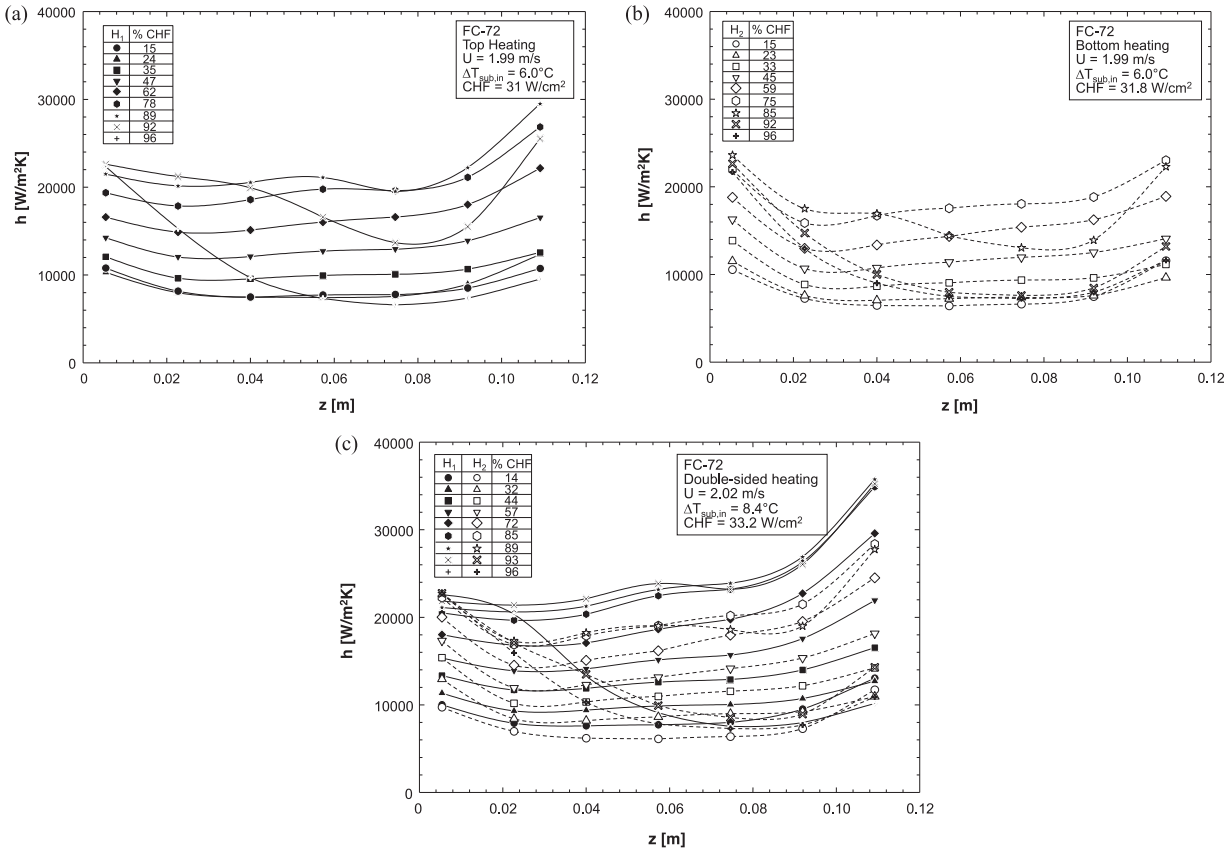

Fig. 13. Variation of local heat transfer coefficient along the channel with increasing heat flux for U = 1.99–2.02 m/s and (a) top wall heating, (b) bottom wall heating, and (c) double-sided heating.

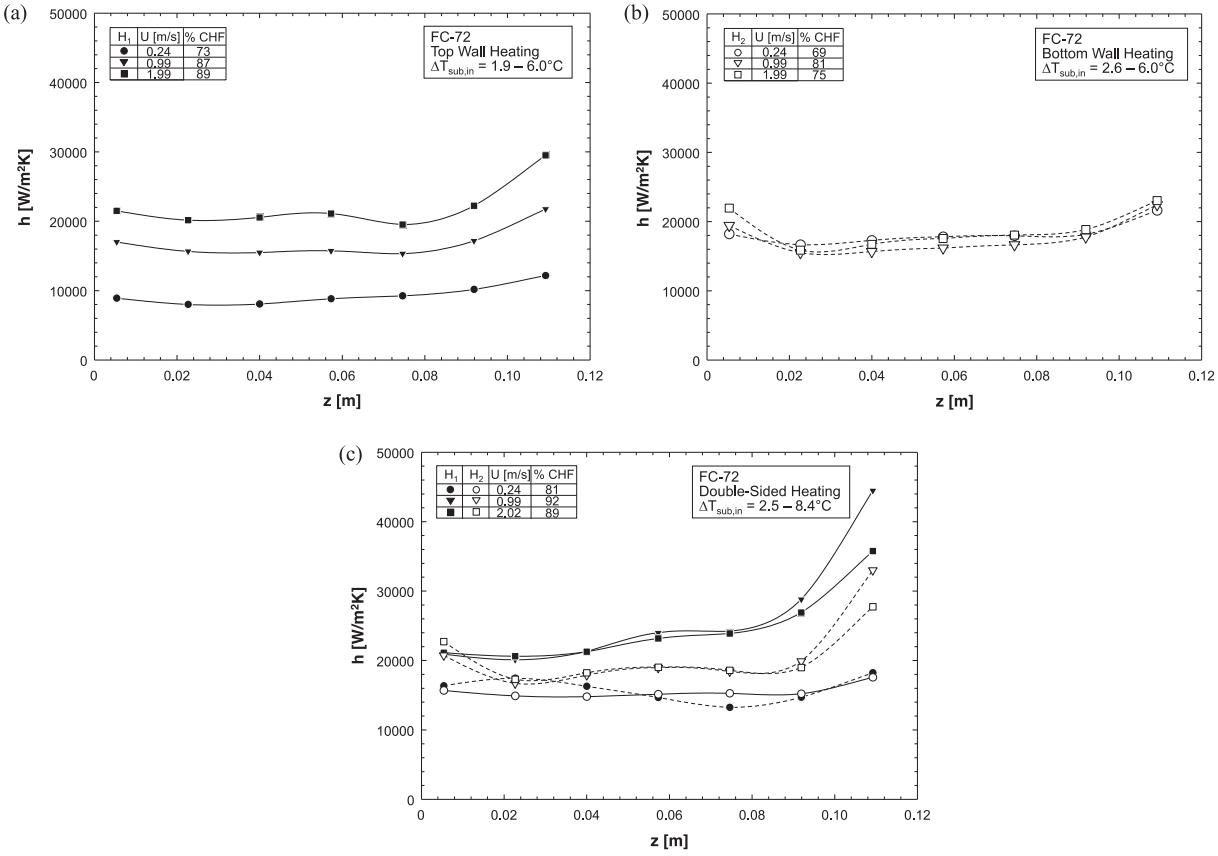

Fig. 14. Variation of local heat transfer coefficient along the channel for different velocities for (a) top wall heating, (b) bottom wall heating and (c) double-sided heating.

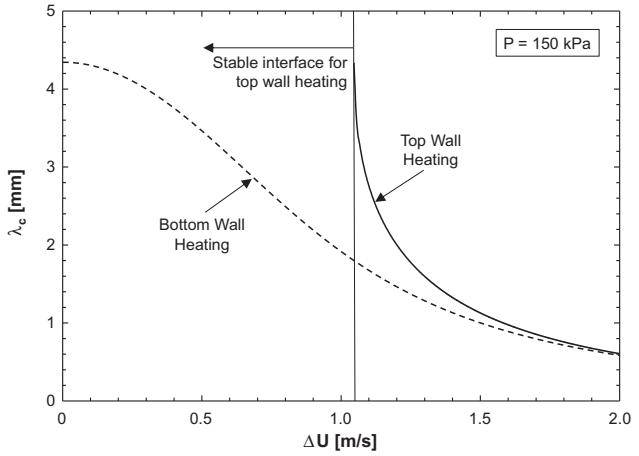

Fig. 15. Variation of critical wavelength with velocity difference between the vapor and liquid layers for top wall heating and bottom wall heating.

decreasing monotonically with increasing ΔU. This implies this interface will always ensure the formation of wetting fronts, which explains the relatively high CHF values for bottom wall heating. Fig. 15 also points to convergence of critical wavelengths for top wall heating and bottom wall heating starting around ΔU = 1.5 m/s. Mathematically, this is the result of the inertia term under the radical in Eq. (3) becoming much larger than the gravity term, *i.e.*, when inertia term begins to negate any gravity influences. This is also the velocity range where interfacial behavior and CHF values become identical for top wall heating and bottom wall heating. These trends are confirmed by re-examining the CHF trends in Fig. 9(a) and (b), where very low velocities yield large differences in CHF values between top wall heating and bottom wall heating, compared to nearly equal CHF values for velocities in excess of 1.5 m/s.

The importance of interfacial behavior to CHF for different surface orientations point to the need for more sophisticated diagnostic tools to better characterize mass, momentum and heat transfer across the wavy interface. A key challenge with such measurements is the small size of the flow channel. However, developments in both micro-particle image velocimetry [27] and the use of micro liquid layer thickness and temperature profile probes [28] provide ample opportunities for researchers to accomplish these goals in future studies.

5. Conclusions

This study explored flow boiling of FC-72 along a rectangular channel that is fitted with top and bottom heating walls that could be individually activated. Three heating configurations were studied: top wall heating, bottom wall heating and double-sided heating. High-speed video imaging was used to identify dominant interfacial characteristics for each configuration for inlet velocities ranging from 0.11 to 2.02 m/s. The heating walls were fitted each with a series of thermocouples to track axial variations of both wall temperatures and heat transfer coefficients. Key findings from the study are as follows:

(1) Flow visualization proves gravity effects are dominant for velocities below 0.49 m/s. Top wall heating at low velocities allows buoyancy to accumulate vapor along the heated wall, leading to unusually low CHF values. For bottom wall

heating, buoyancy aids in vapor removal and liquid replenishment of the heated wall, resulting in much higher CHF values. For double-sided heating, interfacial behavior combines the interfacial behaviors of top wall and bottom wall heating. For $U = 0.99–2.02$ m/s, a wavy vapor layer is generated along the heated walls for all three configurations. Near CHF, the wall is covered mostly with vapor, while liquid could replenish the wall in wetting fronts corresponding to the wave troughs. For double-sided heating, increasing velocity promotes greater symmetry between interfacial behaviors along the opposite walls.

(2) CHF for top wall heating is lower than for bottom wall heating, especially for low velocities. CHF for double-sided heating falls between those for the other configurations at low velocities, but is highest for $U \geqslant 0.99$ m/s because of flow acceleration caused by greater vapor accumulation with both walls activated. Overall, CHF values for all three configurations converge to one another above $U = 1.5$ m/s. This convergence is clearly the result of high inertia negating the influence of gravity.

(3) For all three heating configurations, the heat transfer coefficient generally decreases in the upstream region of the heated wall and increases in the downstream region. High values at the inlet are attributed to initiation of a thermal boundary layer in liquid at low heat fluxes, and discrete bubble nucleation at higher fluxes. The degradation in about the upstream half of the heated wall is attributed to vapor bubble coalescence into large vapor patches that partially insulate the heated wall. The downstream enhancement is the result of fluid acceleration due to increased vapor void, which is most pronounced for double-sided heating.

(4) Interfacial instability theory provides important insight into the influence of velocity on CHF for top wall versus bottom wall heating. For top wall heating, the interface is stable at low velocities, causing the vapor layer to accumulate against the top wall with no opportunity to form wetting fronts, which explains the very low CHF values for this configuration. The interface for top wall heating becomes unstable for $\Delta U > 1.03$ m/s, allowing wetting fronts to be formed and resulting in improved cooling. For bottom wall heating, the interface is always unstable, favoring wetting front formation. Instability theory shows that inertia dwarfs gravity around $\Delta U = 1.5$ m/s, causing critical wavelengths for top wall and bottom wall heating to converge. This is also the velocity range where CHF values for top wall and bottom wall heating converge.

Conflict of interest

None declared.

Acknowledgments

The authors are grateful for the support of this project by the National Aeronautics and Space Administration (NASA) under grant no. NNX13AB01G. Support was also provided by the NASA Office of the Chief Technologist's Space Technology Research Fellowship grant no. NNX11AM81H. The authors thank David F. Chao, James D. Wagner, Rochelle I. May, Daniel M. Houser and Bruce J. Frankenfield of the NASA Glenn Research Center for their technical assistance.

References

[1] I. Mudawar, Two-phase micro-channel heat sinks: theory, applications and limitations, J. Electron. Packag. – Trans. ASME 133 (2011) 041002-2.
[2] D.D. Hall, I. Mudawar, Ultra-high critical heat flux (CHF) for subcooled water flow boiling – II. High-CHF database and design parameters, Int. J. Heat Mass Transfer 42 (1999) 1429–1456.
[3] T.C. Willingham, I. Mudawar, Forced-convection boiling and critical heat flux from a linear array of discrete heat sources, Int. J. Heat Mass Transfer 35 (1992) 2879–2890.
[4] T.N. Tran, M.W. Wambsganss, D.M. France, Small circular- and rectangular-channel boiling with two refrigerants, Int. J. Multiphase Flow 22 (1996) 485–498.
[5] H.J. Lee, S.Y. Lee, Heat transfer correlation for boiling flows in small rectangular horizontal channels with low aspect ratios, Int. J. Multiphase Flow 27 (2001) 2043–2062.
[6] L. Lin, R. Ponnappan, Heat transfer characteristics of spray cooling in a closed loop, Int. J. Heat Mass Transfer 46 (2003) 3737–3746.
[7] M. Visaria, I. Mudawar, Theoretical and experimental study of the effects of spray inclination on two-phase spray cooling and critical heat flux, Int. J. Heat Mass Transfer 51 (2008) 2398–2410.
[8] Y. Katto, M. Kunihiro, Study of the mechanism of burn-out in boiling system of high burn-out heat flux, Bull. JSME 16 (1973) 1357–1366.
[9] D.C. Wadsworth, I. Mudawar, Enhancement of single-phase heat transfer and critical heat flux from an ultra-high-flux simulated microelectronic heat source to a rectangular impinging jet of dielectric liquid, J. Heat Transfer – Trans. ASME 114 (1992) 764–768.
[10] M.K. Sung, I. Mudawar, Experimental and numerical investigation of single-phase heat transfer using a hybrid jet impingement/micro-channel cooling scheme, Int. J. Heat Mass Transfer 49 (2006) 682–694.
[11] M.K. Sung, I. Mudawar, Correlation of critical heat flux in hybrid jet impingement/micro-channel cooling scheme, Int. J. Heat Mass Transfer 49 (2006) 2663–2672.
[12] F.P. Chiaramonte, J.A. Joshi, Workshop on critical issues in microgravity fluids, transport, and reaction processes in advanced human support technology – final report, NASA TM-2004-212940, 2004.
[13] The National Academies, Recapturing a Future for Space Exploration: Life and Physical Sciences Research for A New Era, National Academies Press, Washington, DC, 2011.
[14] S.S. Kutateladze, A.I. Leont'ev, Some applications of the asymptotic theory of the turbulent boundary layer, in: Proc. Third Int. Heat Transfer Conf., Chicago, Illinois, vol. 3, 1966, pp. 1–6.
[15] L.S. Tong, Boundary-layer analysis of the flow boiling crisis, Int. J. Heat Mass Transfer 11 (1968) 1208–1211.
[16] W. Hebel, W. Detavernier, M. Decreton, A contribution to the hydrodynamics of boiling crisis in a forced flow of water, Nucl. Eng. Des. 64 (1981) 443–445.
[17] J. Weisman, B.S. Pei, Prediction of critical heat flux in flow boiling at low qualities, Int. J. Heat Mass Transfer 26 (1983) 1463–1477.
[18] C.H. Lee, I. Mudawar, A mechanistic critical heat flux model for subcooled flow boiling based on local bulk flow conditions, Int. J. Multiphase Flow 14 (1988) 711–728.
[19] C.R. Kharangate, I. Mudawar, M.M. Hasan, Experimental and theoretical study of critical heat flux in vertical upflow with inlet vapor void, Int. J. Heat Mass Transfer 55 (2012) 360–374.
[20] H. Zhang, I. Mudawar, M.M. Hasan, Photographic study of high-flux subcooled flow boiling and critical heat flux, Int. J. Heat Mass Transfer 34 (2007) 653–660.
[21] C.R. Kharangate, I. Mudawar, M.M. Hasan, Photographic study and modeling of critical heat flux in horizontal flow boiling with inlet vapor void, Int. J. Heat Mass Transfer 55 (2012) 4154–4168.
[22] H. Zhang, I. Mudawar, M.M. Hasan, Experimental and theoretical study of orientation on flow boiling CHF, Int. J. Heat Mass Transfer 45 (2002) 4463–4477.
[23] C. Konishi, I. Mudawar, Investigation of the influence of orientation on critical heat flux for flow boiling with two-phase inlet, Int. J. Heat Mass Transfer 61 (2013) 176–190.
[24] C. Konishi, H. Lee, I. Mudawar, M.M. Hasan, H.K. Nahra, N.R. Hall, J.D. Wagner, R.L. May, J.R. Mackey, Flow boiling in microgravity: Part 1 – Interfacial behavior and experimental heat transfer results, Int. J. Heat Mass Transfer 81 (2015) 705–720.
[25] H. Zhang, I. Mudawar, M.M. Hasan, Flow boiling CHF in microgravity, Int. J. Heat Mass Transfer 48 (2005) 3107–3118.
[26] C. Konishi, H. Lee, I. Mudawar, M.M. Hasan, H.K. Nahra, N.R. Hall, J.D. Wagner, R.L. May, J.R. Mackey, Flow boiling in microgravity: Part 2 – Critical heat flux interfacial behavior, experimental data, and model, Int. J. Heat Mass Transfer 81 (2015) 721–736.
[27] W. Qu, I. Mudawar, S.-Y. Lee, S.T. Wereley, Experimental and computational investigation of flow development and pressure drop in a rectangular micro-channel, J. Electron. Packag. – Trans. ASME 128 (2006) 1–9.
[28] T.H. Lyu, I. Mudawar, Statistical investigation of the relationship between interfacial waviness and sensible heat transfer to a falling liquid film, Int. J. Heat Mass Transfer 34 (1991) 1451–1464.